Sustainable Energy & Fuels

Engineering Block Co-polymer Anion Exchange Membrane Domains for Highly Efficient Electrode-Decoupled Redox Flow batteries

Journal:	*Sustainable Energy & Fuels*
Manuscript ID	SE-ART-04-2021-000543.R1
Article Type:	Paper
Date Submitted by the Author:	19-May-2021
Complete List of Authors:	Wang, Zhongyang; University of Chicago, Pritzker School of Molecular Engineering; Washington University in Saint Louis, Sankarasubramanian, Shrihari; Washington University in St. Louis, Energy, Environment and Chemical Engineering Willey, Jason; Giner Inc Feng, Hongbo; The University of Chicago Xu, Hui; Giner Inc Ramani, Vijay; Washington University in St. Louis, Energy, Environment and Chemical Engineering

Engineering Block Co-polymer Anion Exchange Membrane Domains for Highly Efficient Electrode-Decoupled Redox Flow batteries

Zhongyang Wang[a,12], Shrihari Sankarasubramanian[a,1], Jason Willey[b], Hongbo Feng[c], Hui Xu[b], Vijay Ramani[a,z]

[a] Center for Solar Energy and Energy Storage and Department of Energy, Environmental and Chemical Engineering, Washington University in St. Louis, One Brookings Dr., St. Louis, MO 63130, USA

[b] Giner Inc., Newton, MA 02466, USA

[c] Pritzker School of Molecular Engineering, The University of Chicago, 5640 South Ellis Avenue, Chicago, IL 60637, USA

[z] Corresponding Author's email: ramani@wustl.edu

[1] These authors contributed equally.

[2] Present address: Pritzker School of Molecular Engineering, The University of Chicago, 5640 South Ellis Avenue, Chicago, IL 60637, USA

Abstract

Anion exchange membranes (AEMs) with high permselectivity, chemical stability and mechanical robustness are a key enabling technology for a variety of electrochemical energy conversion and storage systems such as fuel cells, redox flow batteries and water electrolyzers. Herein we examine well understood chemically stable triblock co-polymer AEMs derived by the chloromethylation (CM-) and subsequent trimethylamine (TMA) functionalization of polystyrene-*block*-poly(ethylene-*ran*-butylene)-*block*-polystyrene (SEBS) block co-polymers. We show using small angle X-ray scattering (SAXS) that the introduction of a hydrophobic reinforcement matrix disrupts phase segregation and decreases ionic domain sizes in these AEM separators. The reinforcement matrix simultaneously causes the ultimate tensile strength (UTS) of the reinforced separator to increase by almost 600% compared to the unreinforced form, while maintaining comparable elasticity (*ca.* 500% elongation at break). Such reinforced r-SEBS30-TMA separators enable electrode-decoupled redox flow batteries (ED-RFBs) with significantly improved lifetimes by decreasing per cycle capacity fade from 0.5% to <0.05%. This 10x improvement in *operando* permselectivity opens the door to ED-RFBs employing inexpensive elemental actives achieving decades-long usable lifespans.

Introduction

The increasing deployment of renewable energy sources and associated energy storage using batteries or H_2/H_2 carriers[1] are compelling future routes towards a carbon-neutral energy ecosystem. The rapid adoption and deployment of renewable energy sources is increasingly an economical inevitability [2] with the levelized costs of terrestrial solar and wind installations being much lower than conventional coal, nuclear or oil-based power plants. These developments require suitable energy storage solutions, and a promising solution is the use of redox-flow batteries (RFBs). Compared with other electricity energy storage systems such as rechargeable metal-air batteries and metal-ion batteries, RFBs have been demonstrated to have competitive features including low storage capacity cost, long battery lifetime, and high energy efficiency.[3-5] Many RFB systems have drawn researchers' attention such as all-vanadium,[6-9] all-uranium,[10] and electrode-decoupled (ED-)RFBs (i.e. RFBs that use different redox couples at the anode and the cathode) such as iron-vanadium,[11, 12] vanadium-cerium,[13-15] iron-chromium,[16, 17] zinc-nickel,[18] zinc-cerium,[19-21] and zinc-bromine.[22, 23] The introduction and assessment of these different RFB chemistries also introduces the issue of identifying comparison metrics to assess these systems. Yao *et al.* illustrates the various pitfalls in reporting RFB data and comparing different systems.[45] A comprehensive program examining these various RFB chemistries in light of technical and techno-economic performance is needed to deploy commercially viable systems.

The all-vanadium redox flow battery (VRFB) is the most commercially mature system due to its long-life, mild operating temperature range[24] and because the intermixing of the anolyte and catholyte results only in an easily remedied loss in capacity and energy efficiency in the VRFB.[25] Nevertheless, VRFBs suffer from low standard cell voltage (1.26 V) and the oxidative degradation

of hydrocarbon-based membrane separators caused by the vanadium (V) cation requires the use of fluorocarbon-based membranes as separators.

ED-RFBs use anion exchange membrane (AEM) separators (as opposed to cation exchange membranes used in the VRFB) to enable to use of different cationic redox couples at the anolyte and catholyte.[14, 26] The key factor that enables the high performance of the ED-RFB is to equip the ED-RFB with ion exchange separators with high permselectivity. The use of Nafion® or similar cation exchange membranes (CEMs) in these systems is impossible as these CEMs will allow the facile transfer of cations from one electrode to the other, thereby precluding us from realizing a true ED-RFB. As an example of the various approaches adopted to improve permselectivity, Li *et al.* drop casted a layer of Ketjen black carbon on both sides of Nafion® membrane for polysulfide-iodide RFB. [27] Due to the large surface area of the Ketjen black carbon, both polysulfide and polyiodide ions were trapped during the charge-discharge cycle. As the charges accumulated in the carbon, the same anions were prevented from entering the membrane due to the electrostatic repelling effect. At the same time, the Ketjen black carbon added more electronic conductivity and less water uptake to the Nafion® membrane. Li *et al.* were able to operate the polysulfide-iodide RFB with modified Nafion® membrane for 1200 cycles (close to three months) while a maximum of 160 hours cycling was obtained for the same RFB with unmodified Nafion®. This work shows a novel approach to improve the permselectivity and prevent excessive water migration that helps to improve the battery performance.

In addition to high permselectivity, the development of mechanically and chemically robust AEMs is also imperative for enabling these systems. [28] Amongst all the possible combinations of redox couples for ED-RFBs, the vanadium-cerium (V-Ce) ED-RFB has relative high cell voltage (the catholyte Ce^{4+}/Ce^{3+} has a standard potential of 1.44 V vs. SHE compared with V^{5+}/V^{4+} at 1 V

vs. SHE), good reversibility and acceptable energy density.[15, 29] A schematic of a typical V-Ce ED-RFB is depicted in **Figure 1**. Yun *et al.* developed cardo-polyetherketone based AEMs for such ED-RFBs and showed that it is possible to achieve separation of the redox active cations over extended periods of time.[15] Employing the same AEM but by modifying the solvation shell around the redox active cations by using methanesulfonic acid as the supporting electrolyte, Sankarasubramanian *et al.* significantly reduced cation cross-over which enabled extended cycling of the V-Ce ED-RFB with no capacity fade.[14] Moving to block co-polymers, Wang *et al*. developed polystyrene-*block*-poly(ethylene-*ran*-butylene)-*block*-polystyrene-based AEMs and employed them as separator in a V-Ce RFB.[13] The separation of the hydrophilic and hydrophobic domains in these separators enable us to tailor the cross-over of the cationic redox active species by changing the ratio of the styrene block (site of the functional group and hydrophilic) to the other hydrophobic blocks.[13] Over 20 charge/discharge cycles, the RFB with the polystyrene-*block*-poly(ethylene-*ran*-butylene)-*block*-polystyrene-based AEM separator with 30 wt.% styrene (hereafter referred to as SEBS30) exhibited 10% capacity fade, while the loss in capacity rose to 15% for the same separator with 35 wt.% styrene (SEBS35) and was about 40% for the benchmark Nafion®212 separator.[13] Therefore, one of the goals of this work is to significantly reduce the capacity fade per cycle from the previously exhibited 0.5% loss in capacity per cycle, which we deem to be unacceptably large for viable commercial application. Another common challenge faced by AEM separators for RFBs is mechanical stability. For example, cardo-polyetherketone-based AEMs exposed *ex situ* to 1.5 M VO_2^+ in 3 M H_2SO_4 at 30 ºC for 60 days led to the ultimate tensile strength of the AEM degrading from 19 MPa to 9 MPa.[6] Thus, a second objective of this study is to improve the AEM's mechanical durability.

The present study integrates a porous, mechanically robust reinforcement matrix made of extended polytetrafluoroethylene (e-PTFE) with the SEBS ionomer to impart its mechanical strength to the separator. The reinforcement matrix was found to disrupt phase-segregation of the SEBS block co-polymer as seen from small angle X-ray scattering (SAXS) and this effect significantly improved its permselectivity. The reinforced AEMs (r-SEBS-TMA) were prepared and utilized as separators for a V-Ce RFB and the performance of V-Ce ED-RFBs using r-SEBS30-TMA, SEBS30-TMA (30: 70 molar ratio of styrene to rubber), and Nafion® 212 as the separator were compared. The r-SEBS-TMA separators were also found to be stable in acidic RFB electrolytes at 40^0C, ensuring that they can be deployed under practical operational conditions in RFBs. After 40 charge/ discharge cycles, a V-Ce RFB with r-SEBS30-TMA as separator was able to maintain 98% of its initial capacity (0.05 % capacity loss per cycle) with no loss in AEM separator mechanical strength.

Experimental

Materials

Chlorobenzene (99.5%), 1,2-dichlorobenzene (analytical standard), tin(IV) chloride (99.995%), chlorotrimethylsilane (99%), chloroform (99.5%), methanol (99.9%), paraformaldehyde (99.5%), silver nitrate (0.1N), potassium thiocyanate (0.1N), sodium nitrate (99%), chloroform-d (99.96%), 1-methyl-2-pyrrolidinone (99.7%), trimethylamine solution (31%-35% weight percent in ethanol), sulfuric acid (99.999%), vanadium (IV) oxide sulfate (97%) and cerium (IV) sulfate (97%) were purchased from Sigma Aldrich. SEBS (M_n=118000 g/mol, 30:70 molar ratio of styrene to rubber) was obtained from Sigma Aldrich. Expanded PTFE (ePTFE) were purchased from Donaldson Company Inc. (properties listed in **Table S1**) and the PTFE sheet to fabricate the non-porous base for separator preparation was obtained from McMaster-Carr.

Fabrication of reinforced AEMs (r-SEBS30-TMA)

The detailed method of synthesizing and characterizing chloromethylated SEBS (CMSEBS30) can be found in our previous reports. [13, 30] The ^{1}H-NMR spectrum of CMSEBS30 is shown in **Figure S1**. The obtained CMSEBS30 has a degree of functionalization (DF) value of 0.20, which leads to a theoretical IEC of 1.68 mmol/g. The method of impregnating CMSEBS30 and an illustration of chemical reactions for chloromethylation and functionalizing CMSEBS30 are shown in **Figure 2. (a)& (b)**. The base used to support the ePTFE reinforcement layer was made of PTFE. A hollow depression was machined into this sheet with a lip on all four edges with a height of 2 mm. The depression was partially filled with 10mL of 5% CMSEBS30 in 1,2-dichlorobenzene solution, the ePTFE layer was laid on top of this layer and an additional 10mL of the CMSEBS30 solution was cast on top. 1,2-dichlorobenzene wets the ePTFE and hence the solution filled out the pores of the ePTFE as seen from the cross-sectional SEM images in **Figure S2**. As a visual confirmation, the ePTFE substrate, which is normally opaque white, becomes clear when filled with polymer. Finally, the ePTFE reinforced membrane was dried at 60 °C on a hot plate and hot-pressed at 110 °C and 300 psi for five minutes to ensure surface uniformity. The reinforced, chloromethylated SEBS30 membrane was then functionalized with the TMA cation as detailed by us previously.[13] The thickness of the SEBS30-TMA and r-SEBS30-TMA membranes are 72 μm and 50 μm, respectively.

Membrane characterization

The membrane characterization methods detailed below follow the procedures we have previously detailed.[13]

Ion exchange capacity (IEC) -The IECs of membranes in chloride form (i.e. ion exchanged to ensure the mobile anions are Cl^- ions) were determined by the argentometric Volhard titration method.[31] A vacuum dried SEBS-based AEM in the chloride form (dried at < 0.1 inHg at 60 °C

for 12 hours) was weighed (about 0.1 g) and immersed in 20 mL of 1 M sodium nitrate for 48 h at room temperature. Subsequently, 5.0 mL of 0.1 M silver nitrate (an excess being added to ensure the complete precipitation of the chloride) was added to precipitate the chloride ions with a white silver chloride precipitate being observed if the membrane had any IEC. Quantification was carried out by titration with 0.1 M potassium thiocyanate (0.1 M KSCN, standard solution) using 2-3 drops of 11 wt% iron (III) nitrate in DI water as indicator with the end point being a color change from a light orange to a medium-dark orange color. A control sample was prepared by mixing 20 mL of 1 M $NaNO_3$ with 5.0 mL of 0.1 M $AgNO_3$ and 2-3 drops of 11wt% of $Fe(NO_3)_3$ and titrated with 0.1 M KSCN. The difference in volume used to titrate the control solution and the sample solution was used for calculating the IEC (see equation [1]):

$$\mathrm{IEC_{Cl^-}}\ [\mathrm{mmol\ g^{-1}}] = \frac{(\mathrm{Vol_{cont.}} - \mathrm{Vol_{test}}) \cdot 100\ \mathrm{mM\ KSCN}}{\mathrm{Wt_{dry}}} \qquad [1]$$

Where, IEC_{Cl^-} was the experimental ion-exchange capacity (mmol g^{-1}); $Vol_{cont.}$ was the volume of 0.1 M KSCN used to titrate the control sample (L); $Vol_{test.}$ was the volume of 0.1 M KSCN used to titrate the sample (L); and Wt_{dry} was the weight of the AEM (g)

Ionic conductivity -In-plane ionic conductivity measurements were carried out in a 4-point conductivity cell (BT-110, Scribner Associates) using electrochemical impedance spectroscopy (EIS) to measure the resistance. A 1 cm × 3 cm membrane was placed in the PTFE conductivity cell in contact with the 4 platinum electrodes and immersed in a temperature-controlled DI water bath. A Gamry series G750 potentiostat was used to measure the impedance in the frequency range 100kHz to 0.1 Hz. The high frequency resistance was estimated from the Bode plots (corresponding to a phase angle of zero). The membrane conductivity was calculated using equation [2]:

$$\sigma = \frac{L}{R \cdot t \cdot w} \qquad [2]$$

where, σ was the in-plane membrane conductivity (mS cm^{-1}); R was the in-plane membrane resistance (mOhm); t was the membrane thickness (fully hydrated) (cm); w was the membrane width (fully hydrated) (cm); L was the distance between the two inner electrodes (cm).

Mechanical properties - The tensile tests for r-SEBS30-TMA and SEBS30-TMA AEMs were performed using a Q800 differential mechanical analyzer (TA instruments) equipped with a humidity chamber. The membrane sample (approximate dimensions: 50 mm x 5 mm x 0.05 mm) was fixed in a film tension clamp using a torque of 3 lbF x in. The experiments were performed at 25 °C and 100 % RH. The membrane was stretched at 0.5 MPa min^{-1} until the sample broke. The ultimate tensile strength and the elongation at the break point are reported in **Table 1**.

Ion permselectivity and transport numbers - Membrane permselectivity and transport numbers were measured using the membrane potential method in a lab-made diffusion cell. The AEM was clamped between two well-stirred compartments containing different concentrations of the same salt (0.1 M and 0.5 M KCl). Two identical calomel reference electrodes were used to measure the potential difference (E_s (mV)) between the two solutions arising from the different mobilities of chloride and potassium ions through the membrane. The membrane potential was used to calculate the membrane permselectivity (selectivity of the anion exchange membrane towards anions) and the transport numbers (in this case for chloride and potassium). The following equation was used to calculate anion and cation transport numbers and membrane permselectvity:

$$E_m = (2t_- - 1)\left(\frac{RT}{F}\right)\ln\left(\frac{a_A}{a_B}\right) = (t_- - t_+)\left(\frac{RT}{F}\right)\ln\left(\frac{a_A}{a_B}\right) \quad [3]$$

Where t_+ and t_- are the transport numbers for the cation (K^+) and the anion (Cl^-) respectively, a_A and a_B are the activities of the electrolyte (KCl) in the concentrated and diluted compartments separated by the membrane, T is the absolute temperature, R is the gas constant and F is the Faraday constant. The coefficient ($2t_- -1$) is commonly referred as the membrane permselectivity and represents the difference between the transport numbers for anions and cations.[32]

Scanning electron microscopy (SEM)- The AEM separators were subject to cross-sectional SEM imaging (FEI Nova 230) to verify complete functionalization and (in case of r-SEBS-30-TMA) to verify that the pores of the ePTFE reinforcement matrix are filled with the ionomer. The SEM operational parameters were beam energy of 10 kV, chamber pressure of 9×10^{-3} Pa and chamber temperature of 23°C. The cross-sectional AEM samples were obtained by sectioning the AEM samples following freezing dry samples in liquid N_2. The samples, being poorly electrically conducting, were subject to Au sputter coating in a Leica ACE600 high vacuum sputter coater. The cross-sectional samples were subjected to energy dispersive analysis of X-rays (EDAX) mapping for carbon (from the ionomer backbone and functional group), fluorine (from the ePTFE reinforcement) and chlorine (associated with the functional group).

Small angle X-ray scattering (SAXS) - Small angle X-ray scattering measurements were performed on a SAXSLAB GANESHA 300 XL SAXS system equipped with a GeniX 3D Cu Ultra Low Divergence micro focus sealed tube source. The wavelength λ was 1.54 Å. The detector used was hybrid pixel Dectris Pilatus 300K 2D CMOS photon counting detector. Silver behenate was used for calibration of the beam center and the q-range before measurement. The corrected SAXS patterns were azimuthally averaged to obtain one dimensional SAXS profiles. SAXSGUI v2.19 software was used to analyze the data.

Ex-situ permeability test – The permeability of the membrane separator was tested ex-situ using a 10 mL, water-jacketed PermeGear diffusion cell (shown in **ESI Figure S6**) at 40^0C. The temperature was maintained by constantly circulating water from a water bath into the out jacket of the diffusion cell. Samples were taken at the end of 30 days and the concentration of V on the Ce-side and Ce on the V-side was measured using inductive coupled plasma optical emission spectroscopy (ICP-OES).

Inductive coupled plasma optical emission spectroscopy (ICP-OES) – The ICP-OES measurements were carried out using a PerkinElmer Optima 7300DV instrument. The instrument was calibrated with the appropriate PerkinElmer standards containing V and Ce. The standards were diluted using trace metals grade HNO_3 and calibration curves with a linear fit regression coefficient of determination (R^2) of at least 0.99 were obtained. The V measurements were carried out using a scandium internal standard. No internal standard was used for the determination of Ce concentration to avoid interference from the prominent lines of scandium.

Single-cell RFB testing

RFB experiments were carried out in an acid-resistant single cell with an active area of 25 cm^2 (Scribner Inc.) whose schematic is depicted in **Figure 1**. The RFB was assembled by sandwiching the r-SEBS30-TMA AEM (with a thickness chosen to be equivalent to SEBS30-TMA and Nafion®212) between two graphite felt electrodes (SGL Carbon, Sigracell® GFA6) previously activated by heating in an oven at 400 °C for 30 hours.[33, 34] The electrolyte in the negative compartment (200 mL) contained 0.5 M V^{2+} in 1M H_2SO_4. The positive compartment (200 mL) contained 0.5 M Ce^{4+} in 1M H_2SO_4. The active redox species were V^{3+}/V^{2+} in the negative electrode and Ce^{4+}/Ce^{3+} in the positive electrode and their electrode reactions are as follows –

$$V^{3+} + e^- \leftrightarrow V^{2+} \ (E^0 = -0.26 \text{ V}) \qquad [4]$$

$Ce^{4+} + e^- \leftrightarrow Ce^{3+}$ ($E^0 = 1.61$ V) [5]

A redox cell test system (model 857, Scribner Associates, Inc.) comprising a fluid control unit and a potentiostat with impedance spectroscopy capabilities was employed in the experiments. System control and data acquisition employed the Flow Cell software (Version 1.1, Scribner Associates, Inc.). The RFB was charged and discharged at a constant current density of 50 $mAcm^{-2}$ at room temperature (approx. 21 °C). Both solutions were circulated through the electrodes using Cole-Parmer peristaltic pumps at a constant flow rate of 100 mL min^{-1}. The RFB was considered charged once the cell voltage reached 2 V and discharged when the cell voltage dropped below 0.65 V (cutoff voltages).

The current efficiency (CE), voltage efficiency (VE) and energy efficiency (EE) were calculated using the following equations:

$$CE = {Q_d}/{Q_c} \times 100\% \quad [6]$$

$$VE = {E_d}/{E_c} \times 100\% \quad [7]$$

$$EE = CE \times VE \times 100\% \quad [8]$$

where Q_d and Q_c were the discharge and charge capacities (Ah/L), and E_d and E_c were the average charge and discharge voltages respectively.

Results and Discussion

Figures 3. (a) and **(e)** depict the SEM cross-section of SEBS30-TMA and reinforced SEBS-30-TMA (r-SEBS30-TMA) membranes. The distribution of carbon, chlorine, and fluorine across the cross-sectional area of SEBS30-TMA separators is depicted in **Figures 3. (b), (c)** and **(d).** The separator's polymeric backbone and the functional group both contributed to the carbon signal and served as the backdrop for the chlorine and fluorine signals. The uniform chlorine

distribution confirmed the uniformity of the chloromethylation reaction, functionalization, and subsequent chloride ion exchange of the separator. Minimal fluorine (within experimental error) was seen in SEBS-30-TMA as expected for an unreinforced separator with no apparent source of fluorine signals. **Figures 3. (f), (g)** and **(h)** show the distribution of carbon, chlorine, and fluorine inside r-SEBS30-TMA. The strong, evenly distributed signal of fluorine overlapping with carbon across the cross-section of r-SEBS30-TMA provided clear evidence that the SEBS30-TMA solution was able to permeate the pores of the ePTFE reinforcement. The uniform distribution of chlorine across the separator cross-section with intensities (a visual representation of the EDAX signal counts) comparable to that of unreinforced SEBS-30-TMA indicated that the TMA functionalization and subsequent chloride ion exchange was not affected by presence of the ePTFE reinforcement. This explained the minimal change in the IEC and ionic conductivity. The cross-section SEM images with EDAX spectra of SEBS30-TMA, ePTFE reinforcement, and r-SEBS30-TMA membranes are also shown in **Figure S3**.

The properties of the r-SEBS-30-TMA separator are listed in **Table 1** and compared to the unreinforced SEBS-30-TMA. A four-probe conductivity cell was used to determine the chloride ionic conductivities (σ) of SEBS30-TMA and r-SEBS30-TMA membranes (**Figure 4 (a)**). The chloride ionic conductivity of SEBS30-TMA was slightly higher than that of r-SEBS30-TMA at all temperatures. Even at 70 ºC, the chloride ionic conductivity of SEBS30-TMA was 18 mS/cm compared to 16 mS/cm for r-SEBS30-TMA (only a 12% decrease in ionic conductivity). This is attributable to the lower ion exchange capacity (IEC) (1.18 mmol/g) of r-SEBS30-TMA, compared to SEBS30-TMA (1.34 mmol/g). Given this relatively small decrease in conductivity, no significant increase in the resistance of the RFB was expected. Thus, with minimal increase in the ohmic overpotential losses, changes to the voltage and energy efficiencies were also expected to

be small upon transitioning to the reinforced separators. The Arrhenius plot of ln σ vs. inverse temperature for SEBS-based AEMs is shown in **Figure S5**. The activation energy (Ea) for SEBS30-TMA to transport chloride ion in aqueous is 8.21 kJ/mol and for r-SEBS30-TMA is 8.85 kJ/mol. These Ea values are very close to Nafion® membranes (9.6 kJ/mol) mainly due to the fast ion transport in phase segregated domains.[35] The separators were also immersed in representative RFB electrolytes for over 6 weeks at 40^0C. As seen from **Figure 4(b)**, minimal changes in conductivity and IEC were observed over the course of this chemical stability test. The ultimate tensile strength (UTS) of the r-SEBS-30-TMA separator was found to increase almost 600% compared to the unreinforced form while exhibiting comparable elasticity (*ca.* 500% elongation at break) to SEBS30-TMA (**Table 1& Figure S4**). This led us to anticipate increased useful lifespan of the separator under operational conditions. Chen *at al.* synthesized polyphenylsulfone-based AEMs with different IEC values. Varying the IEC values of the AEMs yielded materials with different conductivity to permeability ratios.[36] It is apparent that an AEM with relatively low IEC will induce high ohmic losses and decrease the power output of the cell whereas an AEM with high IEC may result in high crossover of active species. Previously we have demonstrated that it is indeed possible to fine tune the IEC of a separator to decrease water uptake and improve permselectivity.[37] Unfortunately, this approach requires extremely precise control over the extent of the functionalization reaction thus making it impractical for large scale adoption.

Alternatively, we hypothesized that the introduction of a (preferable hydrophobic) reinforcement layer with tortuous pores would in turn decrease cation cross-over through the hydrophilic, anion-conductive channels in our triblock copolymer AEM. The measured permselectivity and transport numbers (**Table 1**) do indicate higher selectivity for the cross-over of the anion, thus indirectly conforming our hypothesis that the introduction of ePTFE

reinforcements alters the phase segregation behavior of SEBS, in turn affecting the conductive ion channel formation in the separator. Higher permselectivity was observed across r-SEBS30-TMA (80%) compared to SEBS30-TMA (73%) with r-SEBS30-TMA demonstrating the same ion transport selectivity as benchmark AEM (Tokuyama A201).[13] We note that these permselectivity values were obtained using singly charged K^+ and Cl^- ions. Permselectivity will improve further with highly charged cationic species like V^{2+}/V^{3+} and Ce^{3+}/Ce^{4+} due to both their higher charge densities and greater difference in diffusivity compared to their counter-ions. The permeability of V and Ce across r-SEBS30-TMA was measured *ex-situ* in a diffusion cell (shown in **ESI Figure S6**) and found to be 1.4% for V and 0.5% for Ce over 30 days using ICP-OES. Thus, we have simultaneously improved both the mechanical properties and *ex-situ* permselectivity. Direct confirmation of any changes in phase segregation was sought using SAXS.

Figure 5. shows the SAXS profile of SEBS30-TMA and r-SEBS30-TMA AEM separators. SEBS30-TMA displayed multiple peaks at q*, $\sqrt{3}$ q*, 2 q*, and 4 q*, suggesting a cylindrical morphology. [38-40] This cylindrical morphology is in agreement with our earlier observations by atomic force microscopy.[30] This self-assembled morphology of the SEBS triblock copolymer is driven by the inherent chemical incompatibility between the styrene blocks and ethylene-co-butylene blocks. However, phase segregation morphology of r-SEBS30-TMA is less obvious than that of SEBS30-TMA due to the disruption of porous PTFE substrate without prominent peaks being observed. Applying the Bragg spacing equation ($d= \frac{2\pi}{q*}$), the primary domain spacing at q*= 0.0176 $Å^{-1}$ was calculated to be 36 nm for SEBS30-TMA while the domain spacing at q*= 0.0207 $Å^{-1}$ was calculated to be 30 nm for r-SEBS30-TMA. The highly ordered scattering peaks of SEBS30-TMA suggest that the long-range grain size of SEBS30-TMA is bigger than that of r-SEBS30-TMA. [41] It also suggests that the defect density of SEBS30-TMA is

potentially much less than that of r-SEBS30-TMA. The bigger grain size and larger domain spacing of SEBS30-TMA result in larger ionic domains than that of r-SEBS30-TMA. The smaller ionic domains of r-SEBS30-TMA results in lower ionic conductivity but higher permselectivity. [42]

Thus, we have demonstrated that the introduction of a porous, hydrophobic ePTFE reinforcement layer inhibits phase segregation and leads to smaller ionic domains in r-SEBS30-TMA compared to SEBS30-TMA. The resultant improvement in *ex-situ* permselectivity was subsequently exploited in a V-Ce ED-RFB. The voltage profiles of the V-Ce ED-RFBS employing SEBS30-TMA, r-SEBS30-TMA and Nafion®-212 (chosen to match the thickness of the AEMs) separators are depicted in **Figure 6**. The open circuit voltage (OCV) is an excellent metric for the permselectivity of a separator in an operating electrochemical cell with lower permselectivity resulting in smaller OCV.[43, 44] Thus, the ED-RFB employing Nafion®-212 cation exchange membrane (CEM), which allows for the facile cross-over of cations, exhibits the lowest OCV amongst all three cells and highest capacity fade over 20 cycles. The change in the OCV can be understood by applying the Nernst equation to the positive and negative electrodes. The half-cell potential for the negative electrode is given by:

$$E_{negative} = E^0 - \frac{RT}{nF}\ln\left(\frac{[V^{2+}]}{[V^{3+}]}\right) \quad (9)$$

Analogously, the half-cell potential for the positive electrode is given by:

$$E_{positive} = E^0 - \frac{RT}{nF}\ln\left(\frac{[Ce^{3+}]}{[Ce^{4+}]}\right) \quad (10)$$

At any given state of charge (SOC), the difference between these two equations predicts the cell OCV. This treatment assumes perfect permselectivity. In reality, V and Ce cross-over modifies

both half-cell potentials (upon accounting for the cross-over species concentrations in the second term on the righthand side of equations (9) and (10)). Thus, the degree of cross-over is indicated by the deviation of the OCV from the ideal, perfectly permselective case and explains the variation in the OCV between the cells employing different separators.

The introduction (by cross-over) of new cations to the anolyte and catholyte respectively also accounts of the observation of a new voltage plateaus in the charge-discharge profiles of the ED-RFB employing Nafion®-212. The OCVs and capacity fade in ED-RFBs employing the AEMs follows the ex-situ permselectivity trends of the AEMs with r-SEBS30-TMA enabling higher OCV and lower capacity fade compared to SEBS30-TMA. **Figure 7** depicts the long-term cycling data for these ED-RFBs. At 20 cycles, SEBS30-TMA exhibited 10% loss in initial capacity (0.5% per cycle) and Nafion®-212 exhibited a 40% loss (2% per cycle). In comparison, the capacity fade for the V-Ce ED-RFB employing r-SEBS30-TMA was 0% within experimental error in the first 20 cycles. Upon further extended cycling to 40 cycles, a 2% loss of capacity was observed. Thus, averaging the capacity losses over the course of the entire 40 cycles, we observed only 0.05% capacity loss per cycle. Other repeats of this experiment resulted in even lower capacity fade values per cycle, leading us to believe that the capacity fade measured may be a result of leakages and/or electrolyte loss by other means rather than due to cross-over. This may also serve to explain the drop in energy efficiency observed in the r-SEBS30-TMA ED-RFB. The decrease in the energy efficiency in the other ED-RFBs correlated to cation cross-over with the cations that cross-over being electro-inactive at their opposite electrode. **Figure 8** depicts the coulombic, voltage and energy efficiencies of the r-SEBS30-TMA ED-RFB. The coulombic efficiency is close to 100% as expected. The drop in voltage efficiency and hence energy efficiency could be attributed to common engineering issues during long-term cell cycling such as electrolyte leakage, ohmic losses

and possible unbalanced states of charge in the anolyte and catholyte upon some loss of either electrolyte.

Figure 9 summarizes the mechanism underlying this improved performance of ED-RFBs employing reinforced separators. As seen in panels (a) and (b), the introduction of the porous reinforcement layer decreases the size of the ion-conductive hydrophilic domains. Upon water uptake when assembled in an electrochemical system, the hydrophilic domain size increase is restricted by the reinforcement layer while unreinforced AEMs take up more water and swell more as seen in panels (c) and (d). Thus, as seen in **Figure 9(e),** an inverse correlation exists between water uptake and permselectivity, and significant improvements in permselectivity are possible (by employing reinforcement layers) even with minimal drops in IEC.

Conclusion

The introduction of reinforcement layers into block co-polymer AEMs results in the disruption and decrease in their ionic domain size. This effect significantly increases permselectivity while simultaneously improving mechanical properties of these separators. SEBS30-TMA AEMs achieve permselectivity values comparable to commercial, benchmark AEMs (Tokuyama A201) upon employing this strategy. Such r-SEBS30-TMA separators significantly improved lifetimes of ED-RFBs by decreasing per cycle capacity fade from 0.5% to <0.05%. This 10x improvement in *operando* permselectivity opens the door to ED-RFBs employing inexpensive elemental actives achieving decades-long usable lifespans.

Author contributions

Z.W. and S.S. synthesized the ionomers, characterized the separators, assembled, and tested them in RFBs. J.W. and H.X produced reinforced separators using the ionomer. Z.W., S.S. and

V.R. analyzed the data and wrote the manuscript. V.R supervised the project, obtained funding and instrumental facilities.

Conflicts of interest

The authors currently have no financial interests that may be perceived to influence the conclusions presented in this work. The authors are seeking intellectual property protections on aspects of one or more technologies described in this report through the Office of Technology and Management (OTM) at Washington University in St. Louis (WUSTL).

Acknowledgements

The authors gratefully acknowledge financial support from the Advanced Research Projects Agency-Energy (ARPA-E), the US Department of Energy under award no. DE-AR0000768 as part of the Integration and Optimization of Novel Ion Conducting Solids (IONICS) program. The authors gratefully acknowledge Washington University in St. Louis McKelvey School of Engineering and the Roma B. & Raymond H. Wittcoff Distinguished University Professorship for enabling this study. We gratefully acknowledge access to instrumentation from the Nano Research Facility (NRF), a member of the National Nanotechnology Infrastructure Network (NNIN), which is supported by the National Science Foundation under Grant No. ECS-0335765.

References

1. J. O. M. Bockris, *Int. J. Hydrogen Energy*, 2013, **38**, 2579-2588.
2. U. S. E. I. Administration, Levelized Cost and Levelized Avoided Cost of New Generation Resources in the Annual Energy Outlook 2018, https://www.eia.gov/outlooks/aeo/pdf/electricity_generation.pdf).
3. G. Li, C. Dang, Y. Hou, F. Dang, Y. Fan and Z. Guo, *Engineered Science*, 2020, **10**, 85-94.
4. C. Hou, B. Wang, V. Murugadoss, S. Vupputuri, Y. Chao, Z. Guo, C. Wang and W. Du, *Engineered Science*, 2020, **11**, 19-30.
5. Y. Lv, L. Zhu, H. Xu, L. Yang, Z. Liu, D. Cheng, X. Cao, J. Yun and D. Cao, *Engineered Science*, 2019, **7**, 26-37.
6. S. Yun, J. Parrondo and V. Ramani, *Journal of Materials Chemistry A*, 2014, **2**, 6605-6615.

7. C. Fujimoto, S. Kim, R. Stains, X. Wei, L. Li and Z. G. Yang, *Electrochem. Commun.*, 2012, **20**, 48-51.
8. S. Kim, M. Vijayakumar, W. Wang, J. Zhang, B. Chen, Z. Nie, F. Chen, J. Hu, L. Li and Z. Yang, *Physical Chemistry Chemical Physics*, 2011, **13**, 18186-18193.
9. M.-s. J. Jung, J. Parrondo, C. G. Arges and V. Ramani, *Journal of Materials Chemistry A*, 2013, **1**, 10458-10464.
10. T. Yamamura, Y. Shiokawa, H. Yamana and H. Moriyama, *Electrochim. Acta*, 2002, **48**, 43-50.
11. W. Wang, S. Kim, B. Chen, Z. Nie, J. Zhang, G.-G. Xia, L. Li and Z. Yang, *Energy & Environmental Science*, 2011, **4**, 4068-4073.
12. W. Wang, Q. Luo, B. Li, X. Wei, L. Li and Z. Yang, *Adv. Funct. Mater.*, 2013, **23**, 970-986.
13. Z. Wang, J. Parrondo and V. Ramani, *J. Electrochem. Soc.*, 2017, **164**, F372-F378.
14. S. Sankarasubramanian, Y. Zhang and V. Ramani, *Sustainable Energy & Fuels*, 2019, **3**, 2417-2425.
15. S. Yun, J. Parrondo and V. Ramani, *ChemPlusChem*, 2015, **80**, 412-421.
16. Y. K. Zeng, T. S. Zhao, L. An, X. L. Zhou and L. Wei, *J. Power Sources*, 2015, **300**, 438-443.
17. Y. K. Zeng, X. L. Zhou, L. An, L. Wei and T. S. Zhao, *J. Power Sources*, 2016, **324**, 738-744.
18. J. Cheng, L. Zhang, Y.-S. Yang, Y.-H. Wen, G.-P. Cao and X.-D. Wang, *Electrochem. Commun.*, 2007, **9**, 2639-2642.
19. P. K. Leung, C. Ponce de León and F. C. Walsh, *Electrochem. Commun.*, 2011, **13**, 770-773.
20. P. K. Leung, C. Ponce-de-León, C. T. J. Low, A. A. Shah and F. C. Walsh, *J. Power Sources*, 2011, **196**, 5174-5185.
21. Z. Xie, D. Zhou, F. Xiong, S. Zhang and K. Huang, *Journal of Rare Earths*, 2011, **29**, 567-573.
22. D. M. Rose and S. R. Ferreira, *SAND2013-2818C, Sandia National Laboratories, Albuquerque, NM (UR), April*, 2013.
23. S. Suresh, T. Kesavan, Y. Munaiah, I. Arulraj, S. Dheenadayalan and P. Ragupathy, *RSC Advances*, 2014, **4**, 37947-37953.
24. G. L. Soloveichik, *Chem. Rev.*, 2015, **115**, 11533-11558.
25. G.-J. Hwang and H. Ohya, *J. Membr. Sci.*, 1997, **132**, 55-61.
26. M. T. Dizaji and W. Li, *Engineered Science*, 2020, **11**, 54-65.
27. Z. Li and Y.-C. Lu, *Nature Energy*, 2021, DOI: 10.1038/s41560-021-00804-x.
28. Z. Wang, S. Sankarasubramanian and V. Ramani, *Current Opinion in Electrochemistry*, 2018, **12**, 240-245.
29. X. Li, H. Zhang, Z. Mai, H. Zhang and I. Vankelecom, *Energy & Environmental Science*, 2011, **4**, 1147-1160.
30. Z. Wang, J. Parrondo and V. Ramani, *J. Electrochem. Soc.*, 2017, **164**, F1216-F1225.
31. C. G. Arges, J. Parrondo, G. Johnson, A. Nadhan and V. Ramani, *J. Mater. Chem.*, 2012, **22**, 3733-3744.
32. N. Lakshminarayaniah, *J. Membr. Biol.*, 1975, **21**, 175-189.
33. B. Sun and M. Skyllas-Kazacos, *Electrochim. Acta*, 1992, **37**, 1253-1260.
34. Y. Li, J. Parrondo, S. Sankarasubramanian and V. Ramani, *The Journal of Physical Chemistry C*, 2019, **123**, 6370-6378.
35. L. Liu, W. Chen and Y. Li, *J. Membr. Sci.*, 2016, **504**, 1-9.
36. D. Chen, M. A. Hickner, E. Agar and E. C. Kumbur, *ACS Applied Materials & Interfaces*, 2013, **5**, 7559-7566.
37. Z. Wang, M. Mandal, S. Sankarasubramanian, G. Huang, P. A. Kohl and V. K. Ramani, *ACS Applied Energy Materials*, 2020, **3**, 4449-4456.
38. J. K. Kim, H. H. Lee, S. Sakurai, S. Aida, J. Masamoto, S. Nomura, Y. Kitagawa and Y. Suda, *Macromolecules*, 1999, **32**, 6707-6717.

39. C. Sinturel, M. Vayer, M. Morris and M. A. Hillmyer, *Macromolecules*, 2013, **46**, 5399-5415.
40. A. D. Mohanty, C. Y. Ryu, Y. S. Kim and C. Bae, *Macromolecules*, 2015, **48**, 7085-7095.
41. M. Chintapalli, X. C. Chen, J. L. Thelen, A. A. Teran, X. Wang, B. A. Garetz and N. P. Balsara, *Macromolecules*, 2014, **47**, 5424-5431.
42. G. M. Geise, M. A. Hickner and B. E. Logan, *ACS Applied Materials & Interfaces*, 2013, **5**, 10294-10301.
43. Z. Wang, J. Parrondo, C. He, S. Sankarasubramanian and V. Ramani, *Nature Energy*, 2019, DOI: 10.1038/s41560-019-0330-5.
44. G. Braesch, Z. Wang, S. Sankarasubramanian, A. Oshchepkov, A. Bonnefont, E. Savinova, V. Ramani and M. Chatenet, *Journal of Materials Chemistry A*, 2020, DOI: 10.1039/D0TA06405J.
45. Y. Yao, J. Lei, Y. Shi, F. Ai and Y-C Lu, Nature Energy, 2021, DOI: 10.1038/s41560-020-00772-8

Figure captions

Figure 1. Schematic of a typical V-Ce redox flow battery.

Figure 2. (a) Lab-scale process to prepare r-SEBS membranes and **(b)** reaction scheme for functionalizing SEBS triblock copolymer to SEBS with quaternary ammonium (SEBS-TMA).

Figure 3. Scanning electron microscopy showing **(a)** cross-section of a SEBS-TMA membrane, EDAX mapping of the cross-section for **(b)** carbon, **(c)** chlorine, **(d)** fluorine; **(e)** cross-section of a r-SEBS-TMA membrane, EDAX mapping of the cross-section for **(f)** carbon, **(g)** chlorine, **(h)** fluorine

Figure 4. (a) In-plane chloride ion conductivity of r-SEBS30-TMA and SEBS30-TMA; **(b)** representative acidic stability of r-SEBS-based separators over the course of continuous immersion in 1M acid solution at 40^0C.

Figure 5. SAXS profiles for SEBS30-TMA and r-SEBS30-TMA measured at room temperature. The data is plotted as logarithm intensity as a function of q.

Figure 6. V-Ce RFB voltage profiles for a variety of membranes. **(a)** Cycle 1, **(b)** Cycle 20.

Figure 7. V-Ce RFB cycling performance for a variety of membranes. **(a)** normalized capacity over cycling, **(b)** energy efficiency over cycling.

Figure 8. Electrode-decoupled V-Ce RFB efficiencies with r-SEBS-TMA membrane separator.

Figure 9. Mechanism of improved permselectivity in reinforced separators. **(a)** block copolymer separator in dry state, **(b)** block copolymer separator after water imbibition, **(c)** reinforced block copolymer separator in dry state, **(d)** reinforced block copolymer separator after water imbibition, and **(e)** correlation between IEC, water uptake and permselectivity for r-SEBS30-TMA, SEBS30-TMA and SEBS35-TMA (SEBS30-TMA and SEBS35-TMA data taken from ref. 22).

Table 1. Properties of r-SEBS30-TMA and SEBS30-TMA fabricated in this work

	r-SEBS30-TMA	SEBS30-TMA
Experimental IEC (mmol/g)	1.16 ± 0.1	1.35 ± 0.02
Chloride conductivity (@70 ºC, mS/cm)	16 ± 2.6	18 ± 3
Ultimate tensile stress (MPa)	17 ± 2	3.1 ± 0.6
Elongation at break (%)	500 ± 10	536 ± 7
Permselectivity (%)	80	73
Transport number (t_{Cl^-}: t_{K^+})	(0.9:0.1)	(0.87:0.13)

Note. Data for SEBS30-TMA was taken from our previous report for comparison purposes.[13]

Figures

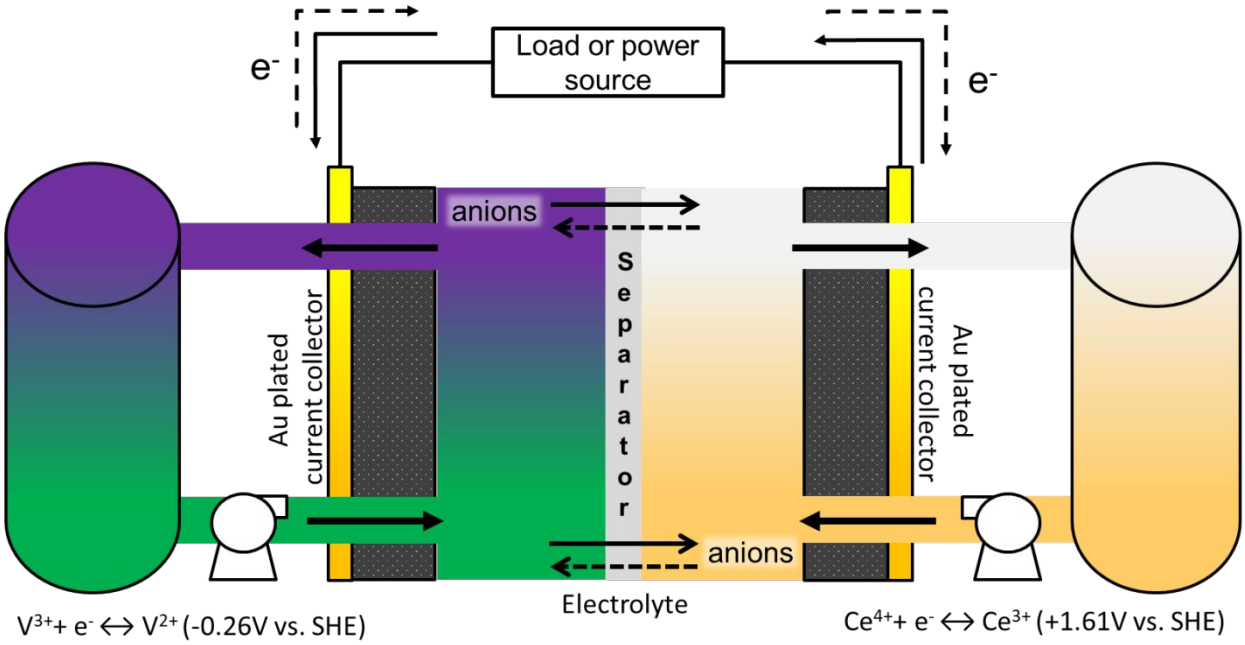

Figure 1. Schematic of a typical electrode-decoupled redox flow battery. A V-Ce chemistry is depicted here. The flow of electrons and anions during the charging process is depicted with solid lines while the flow direction during the discharge process is depicted with dashed lines.

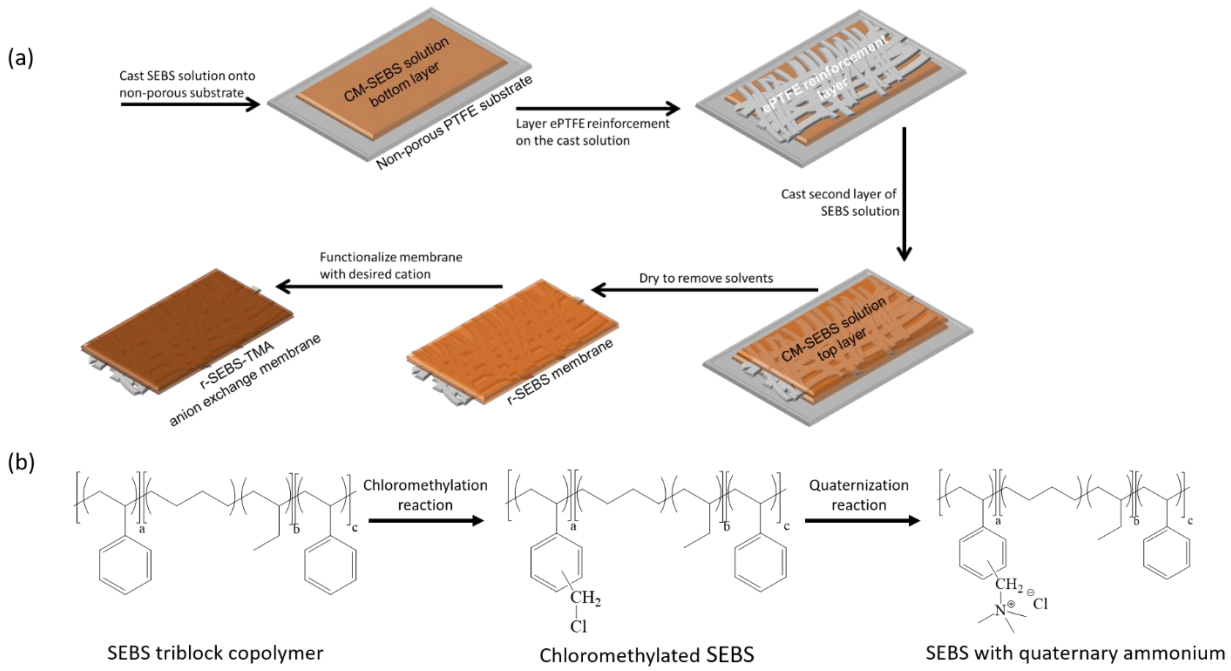

Figure 2. (a) Lab-scale process to prepare r-SEBS membranes and **(b)** reaction scheme for functionalizing SEBS triblock copolymer to SEBS with quaternary ammonium (SEBS-TMA).

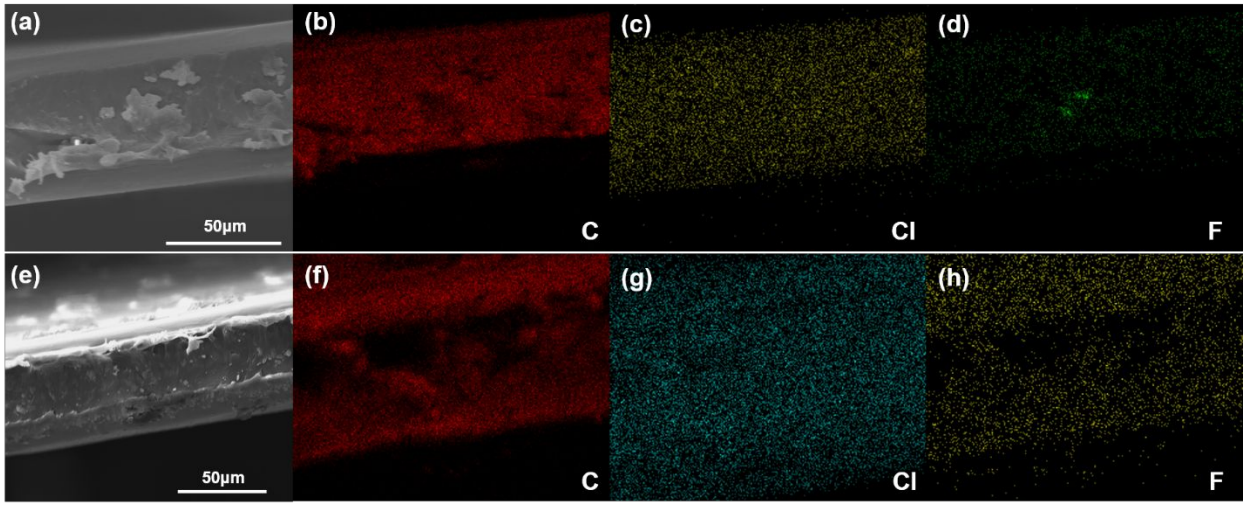

Figure 3. Scanning electron micrographs showing **(a)** cross-section of a SEBS30-TMA membrane, EDAX mapping of the cross-section for **(b)** carbon, **(c)** chlorine, **(d)** fluorine; **(e)** cross-section of a r-SEBS30-TMA membrane, EDAX mapping of the cross-section for **(f)** carbon, **(g)** chlorine, **(h)** fluorine.

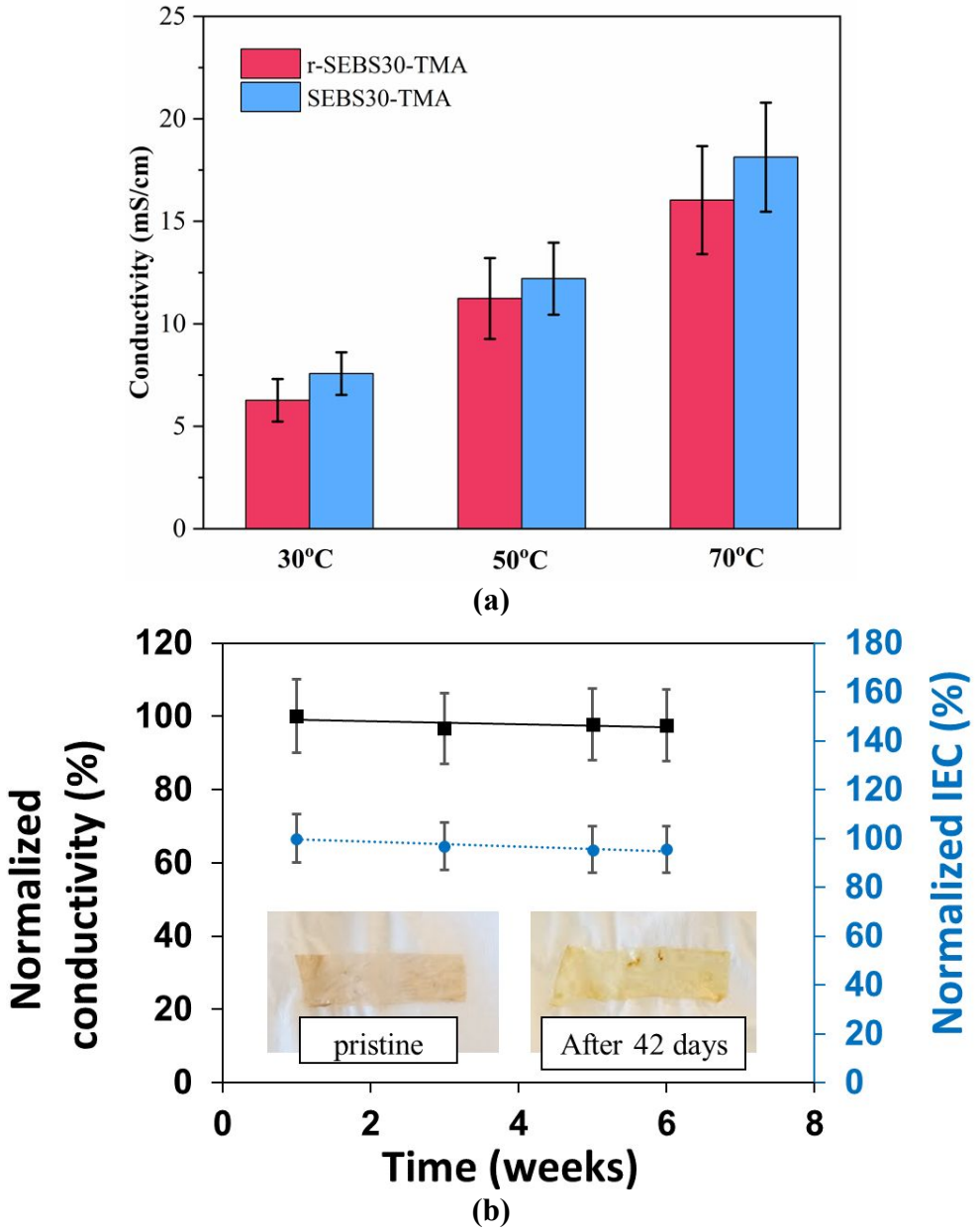

Figure 4. (a) In-plane chloride ion conductivity of r-SEBS30-TMA and SEBS30-TMA; **(b)** representative acidic stability of r-SEBS-based separators over the course of continuous immersion in 1M acid solution at 40^0C.

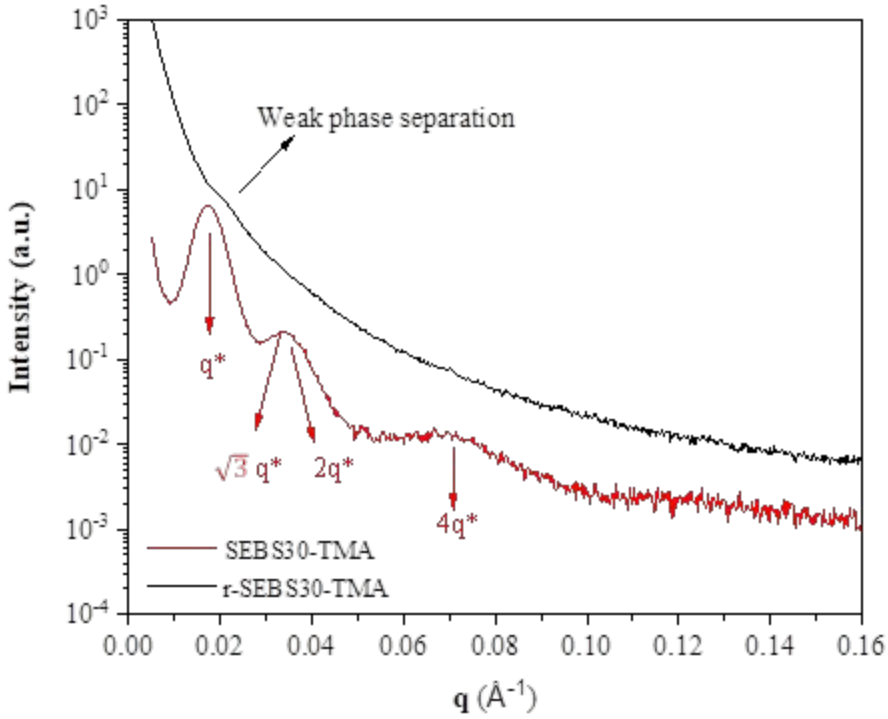

Figure 5. SAXS profiles for SEBS30-TMA and r-SEBS30-TMA measured at room temperature. The data is plotted as logarithm intensity as a function of q.

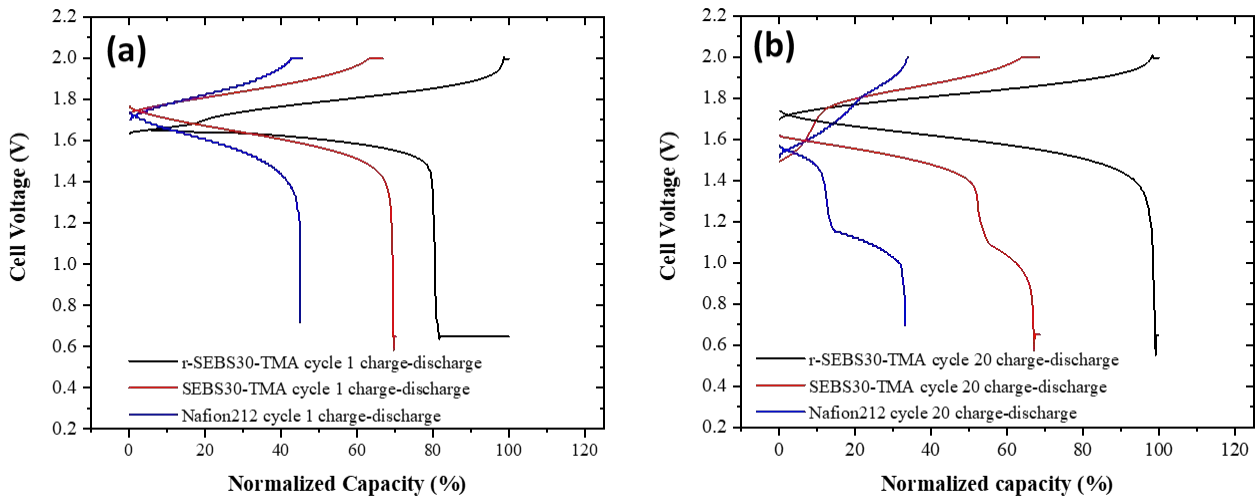

Figure 6. V-Ce RFB voltage profiles for a variety of membranes. **(a)** cycle 1, **(b)** Cycle 20.

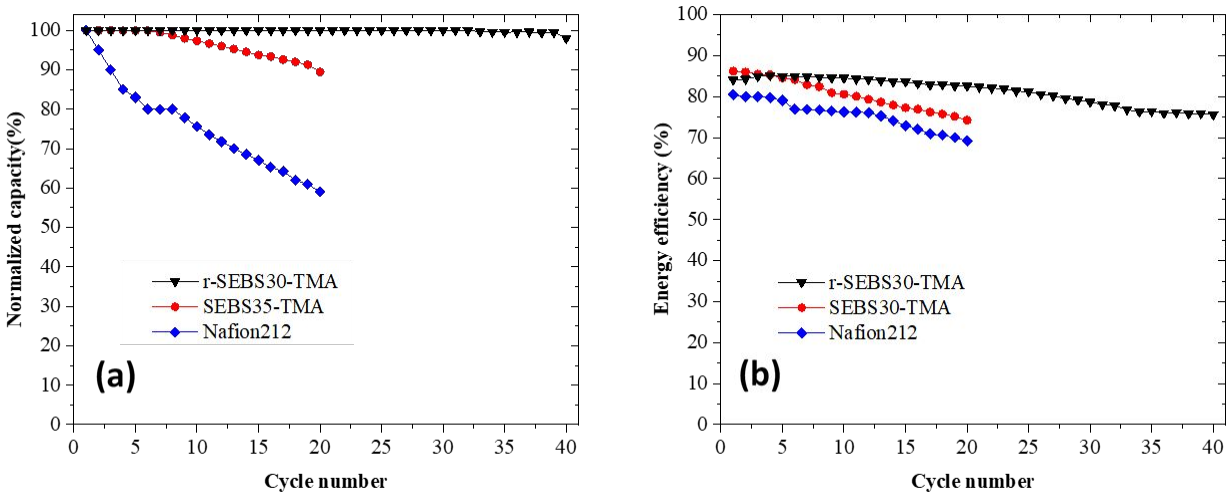

Figure 7. V-Ce RFB cycling performance for a variety of membranes. **(a)** normalized capacity over cycling, **(b)** energy efficiency over cycling.

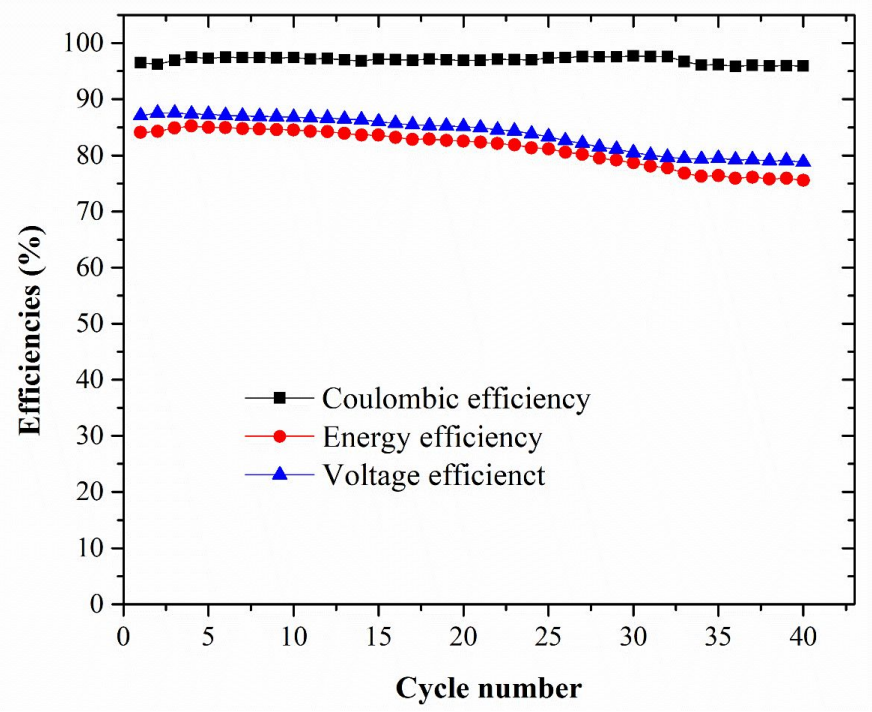

Figure 8. Electrode-decoupled V-Ce RFB efficiencies with r-SEBS-TMA membrane separator.

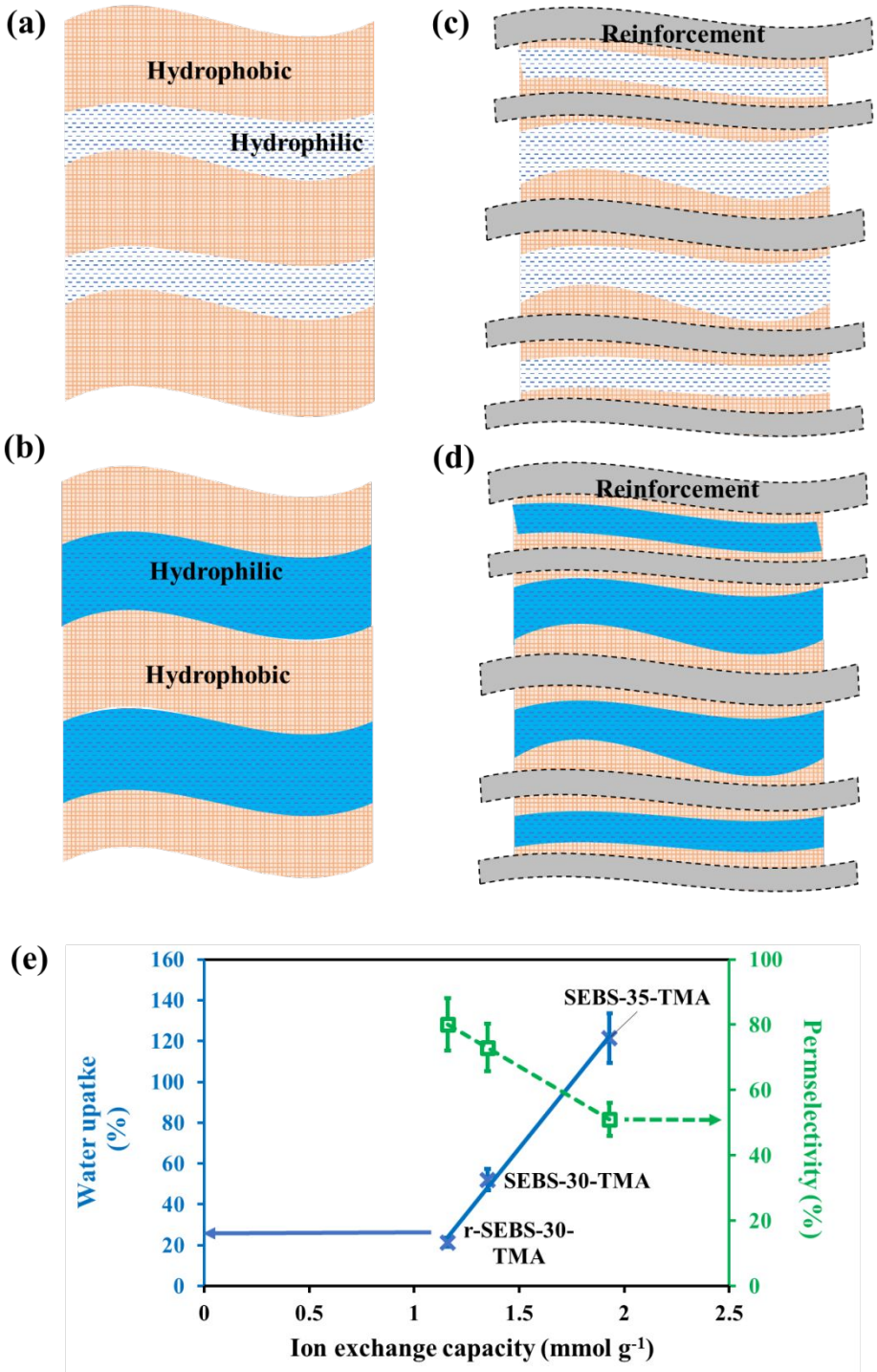

Figure 9. Mechanism of improved permselectivity in reinforced separators. **(a)** block copolymer separator in dry state, **(b)** block copolymer separator after water uptake, **(c)** reinforced block copolymer separator in dry state, **(d)** reinforced block copolymer separator after water uptake, and **(e)** correlation between IEC, water uptake and permselectivity for r-SEBS30-TMA, SEBS30-TMA and SEBS35-TMA (SEBS30-TMA and SEBS35-TMA data taken from ref. 24).